IEEE Access
Multidisciplinary ⋮ Rapid Review ⋮ Open Access Journal

Received 27 July 2023, accepted 21 August 2023, date of publication 24 August 2023, date of current version 30 August 2023.

Digital Object Identifier 10.1109/ACCESS.2023.3308495

RESEARCH ARTICLE

Discrete-Time Noise-Suppression Neural Dynamics for Optical Remote Sensing Image Extraction

YIZHEN XIONG[1], DIFENG WANG[2], DONGYANG FU[1], AND YAN WANG[1]

[1]School of Electronic and Information Engineering, Guangdong Ocean University, Zhanjiang, Guangdong 524088, China
[2]State Key Laboratory of Satellite Ocean Environment Dynamics, Second Institute of Oceanography, Ministry of Natural Resources, Hangzhou, Zhejiang 310012, China

Corresponding authors: Dongyang Fu (fdy163@163.com) and Difeng Wang (dfwang@sio.org.cn)

This work was supported in part by the Key Projects of the Guangdong Education Department under Contract 2019KZDXM019, in part by the Fund of Southern Marine Science and Engineering Guangdong Laboratory (Zhanjiang) under Contract ZJW-2019-08, in part by the High-Level Marine Discipline Team Project of Guangdong Ocean University under Contract 002026002009, in part by the Guangdong Graduate Academic Forum Project under Contract 230420003, in part by the 2019 First Class Discipline Construction Platform Project of Guangdong Ocean University under Contract 231419026, in part by the National Natural Science Foundation of China under Contract 41476157, and in part by the National Key Research and Development Program of China under Grant 2018YFB0505005.

ABSTRACT Optical remote sensing is an important method of observing objects over large areas. Naturally, it is essential to extract the target from optical remote sensing images. Most existing methods, such as thresholding methods and texture analysis-based methods, have some limitations. Additionally, most methods are generally not robust to noise, which tends to affect extraction results to some extent. Thus, how to extract the target object from optical remote sensing images conveniently and robustly is a challenge. To make up for the shortcomings of most methods, a constrained energy minimization (CEM) scheme is applied to extract the target object. Then, a discrete-time noise-suppression neural dynamics (DTNSND) model with an error-accumulation term is proposed to aid the CEM scheme for extracting the target object, which restrains the effects of noises in the extraction process. Theoretical analyses demonstrate that the DTNSND model suppresses noise in diverse noisy environments. Furthermore, numerical simulations are provided to illustrate that the maximal steady-state residual error generated by the DTNSND model is markedly lower than those of comparative algorithms. Finally, extraction experiments, using an optical remote sensing image of the Arctic sea ice as an experimental material, are executed in zero noise and random noise environments, respectively. Comparative results confirm that the DTNSND model is able to extract the remote sensing image stably and accurately in noisy environments, further demonstrating the feasibility of the DTNSND model in practice.

INDEX TERMS Target object extraction, discrete-time noise-suppression neural dynamics (DTNSND) model, constrained energy minimization (CEM) scheme, noise-suppression.

I. INTRODUCTION

Satellite remote sensing technology is an effective method of observing features. Differing from traditional methods, it has the advantages of large scale, real time, and sustainability. One of the most direct way is optical remote sensing, which is characterized by the high spatial resolution of visible and panchromatic images, providing clear spatial texture information of the observation target. Therefore, it is conducive to the intuitive interpretation of remote sensing images.

In order to extract the target object from remote sensing images, many methods are available [1], [2], [3], [4]. Harsanyi and Chang [5] present an orthogonal subspace projection algorithm, which is a hyperspectral image classification technique based on the linear mixed model. Its operator can detect multiple target feature values of interest and classify these images simultaneously. However, this method lacks

The associate editor coordinating the review of this manuscript and approving it for publication was Stefania Bonafoni.

practicality owing to the fact that it requires background spectral information of the target. Subsequently, Ren and Chang [6] investigate a target-constrained interference-minimized filter, which reduces interfering factors and eliminates other uncorrelated signals while detecting the primary target. A system consisting of airborne sensors and various automated algorithms is investigated in [7], whose main role is to project detection points onto high-resolution images through registration algorithms, employing linear discrimination functions and decision surfaces to classify each detected point. However, a large amount of computational resources and time to process high-resolution images are required, and if the processing speed is not fast enough, it may not be able to meet the needs of real-time applications. Thus, this method cannot be widely used. Then, machine learning is applied in the field of optical remote sensing image processing as well, which achieves great results due to its advantages of efficiency, adaptability, accuracy, etc., [8], [9], [10], and [11]. Teng et al. [12] presents a classifier-constrained deep adversarial domain adaptation method for cross-domain semisupervised classification in remote sensing images. In [13], a distributed convolutional neural network is presented and this method performs well in remote sensing image classification. To bridge the research on how to learn embedding spaces under the multilabel assumption, a new graph relation network for multilabel remote sensing scene categorization is presented in [14]. However, machine learning methods require the training and testing of data from the same feature space and distribution [15], [16], [17], and re-collection of data and redesign of models are often necessary when the data distribution changes. Therefore, these methods are difficult to be applied to the target extraction. Moreover, it is worth pointing out that the above methods are not of noise suppression, which may not be effective in noisy environment.

In response to the above issues, a constrained energy minimization (CEM) scheme is considered to extract the target object from remote sensing images in this work. The CEM scheme is a finite impulse response linear filter, which is designed to detect a target of interest and minimize the output energy caused by other unknown signals. This scheme finds applications in various fields [18], [19], [20]. It solely requires the target spectrum without image background information, which is easy to operate and versatile. However, the CEM scheme is not of noise suppression, and thus it is difficult to be employed in noisy environments. Therefore, it is necessary to develope a method to assist the CEM scheme to restrain noises for extracting the target.

The CEM scheme can be transformed into an optimization problem [18]. Several studies in recent years have found that using neural dynamics (ND) to solve optimization problems is effective [21], [22], [23], [24]. In [25], a quadratic-programming (QP) based neural dynamic is presented to complete time-varying tasks. Then, Chen et al. [26] present a multi-constrained ND to synchronously handle multiple types of constraints for the time-dependent nonlinear optimization. Afterwards, Xiao et al. construct two NDs in [27] to decrease the residual error. In addition, Kong et al. [28] establish a generalized varying-parameter recurrent neural network and apply it to control redundant manipulators by solving a QP problem. Although the above algorithms have good computational performance, they are intolerant to noises, which are inevitable in practice. Therefore, a discrete-time noise-suppression neural dynamics (DTNSND) model with an error-accumulation term is proposed to aid the CEM scheme for extracting optical remote sensing images. Theoretical proofs demonstrate that the DTNSND model maintains a high convergence accuracy and strong stability under noise-free and noise conditions. Moreover, experimental results on the extraction of the Arctic sea ice confirm the feasibility of the DTNSND model in practice. The contributions of this paper are listed as follows:

- The DTNSND model is able to improve the solution accuracy under noise-free and noise conditions.
- The DTNSND model is proposed to aid the CEM scheme to extract optical remote sensing images, presenting a new technique to combine the CEM scheme with discrete-time ND.
- Relevant theoretical analyses and experiments are given to demonstrate that the DTNSND model is globally convergent and robust.

II. PROBLEM FORMULATION

The CEM scheme can be written as [29]

$$\begin{aligned} \min \quad & \|S(t)\mathbf{w}(t)+\mathbf{a}(t)\|_2^2/2, && \text{(1a)}\\ \text{s.t.} \quad & N(t)\mathbf{w}(t)=\mathbf{u}(t), && \text{(1b)} \end{aligned}$$

where $\|\cdot\|_2$ denotes L_2-norm operator; $S(t) \in \mathbb{R}^{r\times m}$ and $N(t) \in \mathbb{R}^{n\times m}$ are the real-valued full-rank matrices; $\mathbf{a}(t) \in \mathbb{R}^r$ and $\mathbf{u}(t) \in \mathbb{R}^n$ are the real-valued coefficient vectors; $\mathbf{w}(t)\in \mathbb{R}^m$ is the vector to be solved. Subsequently, a Lagrange formula is constructed as follows:

$$F(\mathbf{w}(t),\mathbf{v}(t),t)=f(\mathbf{w}(t),t)+\mathbf{v}(t)^{\mathrm{T}}(N(t)\mathbf{w}(t)-\mathbf{u}(t)), \quad (2)$$

with

$$\begin{cases} f(\mathbf{w}(t),t)=\|S(t)\mathbf{w}(t)+\mathbf{a}(t)\|_2^2/2,\\ \mathbf{v}(t)=[v_1(t),\cdots,v_n(t)]^{\mathrm{T}}\in\mathbb{R}^n, \end{cases} \quad (3)$$

where superscript $^{\mathrm{T}}$ is the transposition operation, and $\mathbf{v}(t)$ is the Lagrange-multiplier operator vector. Then, the model for solving CEM scheme (1) can be formulated as

$$\begin{cases} \frac{\partial F(\mathbf{w}(t),\mathbf{v}(t),t)}{\partial \mathbf{w}(t)}=\frac{\partial f(\mathbf{w}(t),t)}{\partial \mathbf{w}(t)}+N^{\mathrm{T}}(t)\mathbf{v}(t)=0,\\ \frac{\partial F(\mathbf{w}(t),\mathbf{v}(t),t)}{\partial \mathbf{v}(t)}=N(t)\mathbf{w}(t)-\mathbf{u}(t)=0. \end{cases} \quad (4)$$

Let

$$Q(t) = \begin{bmatrix} Y(t) & N^{\mathrm{T}}(t) \\ N(t) & \mathbf{0}_{n\times n} \end{bmatrix} \in \mathbb{R}^{(m+n)\times(m+n)},$$

$$\mathbf{x}(t) = \begin{bmatrix} \mathbf{w}(t) \\ \mathbf{v}(t) \end{bmatrix} \in \mathbb{R}^{m+n},$$

$$\mathbf{z}(t) = \begin{bmatrix} \mathbf{d}(t) \\ \mathbf{u}(t) \end{bmatrix} \in \mathbb{R}^{m+n}.$$

where $Y(t) = S^{\mathrm{T}}(t)S(t) \in \mathbb{R}^{m\times m}$ and $\mathbf{d}(t) = -S^{\mathrm{T}}(t)\mathbf{a}(t) \in \mathbb{R}^{m}$. Ulteriorly, (4) can be rewritten as

$$Q(t)\mathbf{x}(t) = \mathbf{z}(t). \tag{5}$$

III. DTNSND MODEL DESIGN AND SIMPLIFICATION

An error function is defined as follows:

$$\mathbf{e}(t) = Q(t)\mathbf{x}(t) - \mathbf{z}(t). \tag{6}$$

Then, a design formula with an integral term is introduced as

$$\dot{\mathbf{e}}(t) = -\varsigma\mathbf{e}(t) - \eta\int_0^t \mathbf{e}(\gamma)\mathrm{d}\gamma, \tag{7}$$

where $\varsigma > 0$ and $\eta > 0$. Subsequently, associating (6) and (7) generates

$$\dot{\mathbf{x}}(t) = Q^{-1}(t)\Big(\dot{\mathbf{z}}(t) - \dot{Q}(t)\mathbf{x}(t) - \varsigma\Big(Q(t)\mathbf{x}(t) - \mathbf{z}(t)\Big) - \eta\int_0^t \Big(Q(\gamma)\mathbf{x}(\gamma) - \mathbf{z}(\gamma)\Big)\mathrm{d}\gamma\Big). \tag{8}$$

Further, to discretize the continuous ND, the Euler forward difference formula is introduced:

$$\dot{\mathbf{x}}_k = \frac{\mathbf{x}_{k+1} - \mathbf{x}_k}{\iota}, \tag{9}$$

where ι is the sampling period, and k represents the updating index at time instant $t = k\iota$. Then, the DTNSND model is obtained as

$$\mathbf{x}_{k+1} = \mathbf{x}_k + Q_k^{-1}\Big(\mathbf{z}_k - \mathbf{z}_{k-1} - \mathbf{x}_k(Q_k - Q_{k-1}) - \varsigma\iota(Q_k\mathbf{x}_k - \mathbf{z}_k) - \eta\iota^2\sum_{i=0}^{k}(Q_i\mathbf{x}_i - \mathbf{z}_i)\Big). \tag{10}$$

Let $\Theta = \varsigma\iota$ and $\Delta = \eta\iota^2$. Hereto, equation (10) can be finally represented as

$$\mathbf{x}_{k+1} = \mathbf{x}_k + Q_k^{-1}\Big(\mathbf{z}_k - \mathbf{z}_{k-1} - \mathbf{x}_k(Q_k - Q_{k-1}) - \Theta(Q_k\mathbf{x}_k - \mathbf{z}_k) - \Delta\sum_{i=0}^{k}(Q_i\mathbf{x}_i - \mathbf{z}_i)\Big). \tag{11}$$

In order to facilitate the convergence and robustness analysis of DTNSND model (11), a concise form is derived in the following theorem.

Theorem 1: DTNSND model (11) can be transformed as

$$(1+\Theta)\mathbf{e}_k - \mathbf{e}_{k-1} + \Delta\sum_{i=0}^{k}\mathbf{e}_i + \mathbf{O}(\iota^2) = \mathbf{0}, \tag{12}$$

where $\mathbf{O}(\iota^2)$ *denotes the vector of truncation error* $O(\iota^2)$.

Proof: DTNSND model (11) can be rewritten as

$$Q_k\mathbf{x}_{k+1} = \mathbf{z}_k - \mathbf{z}_{k-1} + Q_{k-1}\mathbf{x}_k - \Theta\mathbf{e}_k - \Delta\sum_{i=0}^{k}\mathbf{e}_i. \tag{13}$$

Then, employing the Taylor expansion expression to the variable in (13) yields

$$\mathbf{x}_{k+1} = \mathbf{x}_k + \iota\dot{\mathbf{x}}_k + \mathbf{O}(\iota^2) \tag{14}$$

and

$$\mathbf{x}_{k-1} = \mathbf{x}_k - \iota\dot{\mathbf{x}}_k + \mathbf{O}(\iota^2). \tag{15}$$

Substituting (14) and (15) into (13) as well as combining the definition of $\mathbf{e}_k$, one has

$$\mathbf{e}_k + \iota Q_k\dot{\mathbf{x}}_k + \mathbf{O}(\iota^2) = \mathbf{e}_{k-1} + \iota Q_{k-1}\dot{\mathbf{x}}_k - \Theta\mathbf{e}_k - \Delta\sum_{i=0}^{k}\mathbf{e}_i. \tag{16}$$

Next, applying the Taylor expansion to Q_k, it has

$$Q_k = Q_{k-1} + \iota\dot{Q}_{k-1} + \Psi(\iota^2), \tag{17}$$

where the matrix $\Psi(\iota^2)$ consists of $O(\iota^2)$. Substituting (17) into (16) and collating gives

$$(1+\Theta)\mathbf{e}_k - \mathbf{e}_{k-1} + \Delta\sum_{i=0}^{k}\mathbf{e}_i + \mathbf{O}(\iota^2) = \mathbf{0}. \tag{18}$$

The proof is complete. □

IV. CONVERGENCE ANALYSIS

The following theorem illustrates the global convergence of DTNSND model (11).

Theorem 2: The residual error $\lim_{k\to\infty}\|\mathbf{e}_k\|_2$ *of DTNSND model (11) is* $O(\iota^2)$.

Proof: In the light of (18), we have

$$(1+\Theta)\mathbf{e}_{k+1} - \mathbf{e}_k + \Delta\sum_{i=0}^{k+1}\mathbf{e}_i + \mathbf{O}(\iota^2) = \mathbf{0}. \tag{19}$$

Let the αth element of $\mathbf{e}_k$ be $\mathbf{e}_k^{\alpha}$. Then, subtracting the αth element of (19) from the αth element of (18) products

$$(1+\Theta+\Delta)\mathbf{e}_{k+1}^{\alpha} = (2+\Theta)\mathbf{e}_k^{\alpha} - \mathbf{e}_{k-1}^{\alpha} + O(\iota^2). \tag{20}$$

Let $\chi_{k+1}^{\alpha} = [\mathbf{e}_{k+1}^{\alpha}, \mathbf{e}_k^{\alpha}]^{\mathrm{T}}$, and (20) can be formulated as

$$\chi_{k+1}^{\alpha} = H\chi_k^{\alpha} + O(\iota^2), \tag{21}$$

with

$$H = \begin{bmatrix} \frac{2+\Theta}{1+\Theta+\Delta} & \frac{-1}{1+\Theta+\Delta} \\ 1 & 0 \end{bmatrix}.$$

From (21), it can be generalized that

$$\begin{aligned}\|\chi_{k+1}^{\alpha}\|_2 &\le \|H\chi_k^{\alpha}\|_2+\|O(\iota^2)\|_2\\ &= \|H\chi_k^{\alpha}\|_2+O(\iota^2)\\ &\le \|H\|_2\|\chi_k^{\alpha}\|_2+O(\iota^2)\\ &\le \|H\|_2\|H\chi_{k-1}^{\alpha}\|_2+\|H\|_2O(\iota^2)+O(\iota^2)\\ &= \|H\|_2\|H\chi_{k-1}^{\alpha}\|_2+O(\iota^2)\\ &\le \|H\|_2^2\|\chi_{k-1}^{\alpha}\|_2+O(\iota^2)\\ &\vdots\\ &\le \|H\|_2^k\|\chi_1^{\alpha}\|_2+O(\iota^2).\end{aligned}$$

The eigenvalues of matrix H are $g_{1,2}=(\Theta\pm\sqrt{\Theta^2-4\Delta}+2)/(2\Theta+2\Delta+2)$. On account of the absolute values of the real part of $g_{1,2}$ are less than 1, it can be obtained that $\lim_{k\to\infty}\|H\|_2^k=0$. Then, the following conclusion is drawn:

$$\lim_{k\to\infty}\|\chi_{k+1}^{\alpha}\|_2\le\lim_{k\to\infty}\|H\|_2^k\|\chi_1^{\alpha}\|_2+O(\iota^2)=O(\iota^2).$$

Therefore, one can further get that the residual error $\lim_{k\to\infty}\|\mathbf{e}_k\|_2$ of DTNSND model (11) is $O(\iota^2)$. The proof is complete. □

V. ROBUSTNESS ANALYSIS

During the target extraction, the presence of noise is strongly related to the quality of the extraction. The random noise is the most common, and thus the following theorem is presented to demonstrate the effectiveness of DTNSND model (11) in finding the theoretical solution under the random noise condition. Meanwhile, DTNSND model (11) with a noise term $\zeta(t)$ can be empressed as follows:

$$\begin{aligned}\mathbf{x}_{k+1}=\mathbf{x}_k+Q_k^{-1}\Big(&\mathbf{z}_k-\mathbf{z}_{k-1}-\mathbf{x}_k(Q_k-Q_{k-1})\\ &-\Theta(Q_k\mathbf{x}_k-\mathbf{z}_k)-\Delta\sum_{i=0}^{k}(Q_i\mathbf{x}_i-\mathbf{z}_i)+\zeta(t)\Big).\end{aligned}\tag{22}$$

Theorem 3: Assuming that DTNSND model (11) to aid the CEM scheme (1) for Arctic sea-ice extraction is affected by the constant noise, the steady-state computing error of DTNSND model (11) is $O(\iota^2)$, regardless of the magnitude of $\zeta(t)=\epsilon$.

Proof: DTNSND model (11) is converted into a linear system (18), and thus the steady-state computing error of the model is the superposition effects of two parts: constant noise $\zeta(t)=\epsilon$ and $\mathbf{O}(\iota^2)$. Thus, from (18), the αth subsystem with a constant noise term can be regarded as

$$(1+\Theta+\Delta)\mathbf{e}_{k+1}^{\alpha}=\mathbf{e}_k^{\alpha}-\Delta\sum_{i=0}^{k}\mathbf{e}_i+\epsilon^{\alpha}.\tag{23}$$

The aforementioned equation can be converted via the Z-transform into the following form:

$$\begin{aligned}&(1+\Theta+\Delta)\Big(z\mathbf{e}^{\alpha}(z)-z\mathbf{e}^{\alpha}(0)\Big)\\ &\quad=\mathbf{e}^{\alpha}(z)-\Delta\frac{\mathbf{e}^{\alpha}(z)}{1-z^{-1}}+\frac{z-1}{z\epsilon^{\alpha}},\end{aligned}\tag{24}$$

where $\mathbf{e}^{\alpha}(0)$ denotes the initial value of $\mathbf{e}^{\alpha}$.The above equation can be further expressed as

$$\mathbf{e}^{\alpha}(z)=\frac{(1+\Theta+\Delta)z(z-1)\mathbf{e}^{\alpha}(0)+z\epsilon^{\alpha}}{(1+\Theta+\Delta)z(z-1)-(z-1)+z\Delta}.\tag{25}$$

The roots of the above equation are $z_{1,2}=(\Theta\pm\sqrt{\Theta^2-4\Delta}+2)/(2\Theta+2\Delta+2)$. Evidently, the absolute values of these roots are not more than 1, that is, (23) is stable. Based on the final value theorem, have

$$\begin{aligned}&\lim_{k\to\infty}\mathbf{e}_k^{\alpha}\\ &=\lim_{z\to1}(z-1)\mathbf{e}^{\alpha}(z)\\ &=\lim_{z\to1}\frac{(z-1)\Big((1+\Theta+\Delta)z(z-1)\mathbf{e}^{\alpha}(0)+z\epsilon^{\alpha}\Big)}{(1+\Theta+\Delta)z(z-1)-(z-1)+z\Delta}\\ &=0.\end{aligned}\tag{26}$$

Thus, the steady-state computing error for subsystem α can be further obtained as $\lim_{k\to\infty}\mathbf{e}_k=0$. Since the truncation error of (20) is $O(\iota^2)$, the steady-state error $\lim_{k\to\infty}\|\mathbf{e}_k\|_2$ of DTNSND model (11) is also $O(\iota^2)$, regardless of the variation of the constant noise $\zeta(t)=\epsilon$. The proof is complete. □

In addition, considering the effect of the random noise, Theorem 4 is given.

Theorem 4: Considering that DTNSND model (11) is disturbed by the bounded random noise $\zeta(t)=\tau\in\mathbb{R}^{m+n}$, its residual error is $\lim_{k\to\infty}\|\mathbf{e}_k\|_2<2(m+n)\sup_{1\le i\le k,1\le\alpha\le(m+n)}|\tau_i^{\alpha}|/(1-\|H\|_2)+O(\iota^2)$.

Proof: DTNSND model (11) is a linear system, and thus the residual error of it can be regarded as a superposition of the impacts of $\zeta(t)=\tau$ and $\mathbf{O}(\iota^2)$. Considering the random noise $\zeta(t)=\tau$ only, it has

$$(1+\Theta+\Delta)\mathbf{e}_{k+1}=\mathbf{e}_k-\Delta\sum_{i=0}^{k}\mathbf{e}_i+\tau.\tag{27}$$

Similar to getting (20), the following equation is available:

$$(1+\Theta+\Delta)\mathbf{e}_{k+1}^{\alpha}=(2+\Theta)\mathbf{e}_k^{\alpha}-\mathbf{e}_{k-1}^{\alpha}+\tau_k^{\alpha}-\tau_{k-1}^{\alpha}.\tag{28}$$

Let $\beta_k^{\alpha}=[\tau_k^{\alpha}-\tau_{k-1}^{\alpha},0]^{\mathrm{T}}$, and equation (28) can be rewritten as

$$\chi_{k+1}^{\alpha}=H\chi_k^{\alpha}+\beta_k^{\alpha}.\tag{29}$$

Therefore, one has

$$\begin{aligned}\|\chi_{k+1}^{\alpha}\|_2 &\le \|H\chi_k^{\alpha}\|_2+\|\beta_k^{\alpha}\|_2\\ &\le \|H\|_2\|\chi_k^{\alpha}\|_2+\|\beta_k^{\alpha}\|_2\\ &\le \|H\|_2\|H\chi_{k-1}^{\alpha}\|_2+\|H\|_2\|\beta_{k-1}^{\alpha}\|_2+\|\beta_k^{\alpha}\|_2\\ &\le \|H\|_2^2\|\chi_{k-1}^{\alpha}\|_2+\|H\|_2\|\beta_{k-1}^{\alpha}\|_2+\|\beta_k^{\alpha}\|_2\\ &\vdots\\ &\le \|H\|_2^k\|\chi_1^{\alpha}\|_2+\|H\|_2^{k-1}\|\beta_1^{\alpha}\|_2+\cdots+\|\beta_k^{\alpha}\|_2\\ &< \|H\|_2^k\|\chi_1^{\alpha}\|_2+\max_{1\le i\le k}\|\beta_i^{\alpha}\|_2/(1-\|H\|_2)\\ &< \|H\|_2^k\|\chi_1^{\alpha}\|_2+2\max_{1\le i\le k}|\tau_i^{\alpha}|/(1-\|H\|_2).\end{aligned}$$

Note that $\lim_{k\to\infty}\|H\|_2^k = 0$, and the aforementioned equation can be rearranged as

$$\|\chi_{k+1}^{\alpha}\|_2 < 2\max_{1\le i\le k}|\tau_i^{\alpha}|/(1-\|H\|_2).$$

Then, the following conclusion can ultimately be drawn

$$\lim_{k\to\infty}\|\mathbf{e}_k\|_2 < 2(m+n)\sup_{1\le i\le k,\,1\le\alpha\le(m+n)}\frac{|\tau_i^{\alpha}|}{1-\|H\|_2}+O(\iota^2).$$

The proof is complete. □

VI. NUMERICAL EXPERIMENTS

In this section, numerical experiments are carried out to demonstrate the excellent robustness and stability of DTNSND model (11). In detail, in the following experiments, the time region $[t_0, t_f]$ of the variable $\mathbf{x}(t)$ is set to be $[0, 20)$ and the matrices $Q(t)$ and $\mathbf{z}(t)$ are defined as

$$\begin{cases} Q(t) = \begin{bmatrix} Q_{11}(t) & Q_{12}(t) & \cdots & Q_{1(m+n)}(t) \\ Q_{21}(t) & Q_{22}(t) & \cdots & Q_{2(m+n)}(t) \\ \vdots & \vdots & \ddots & \vdots \\ Q_{(m+n)1}(t) & Q_{(m+n)2}(t) & \cdots & Q_{(m+n)(m+n)}(t) \end{bmatrix} \in \mathbb{R}^{(m+n)\times(m+n)}, \\ \mathbf{z}(t) = \begin{bmatrix} z_1(t) & z_2(t) & \cdots & z_{m+n}(t) \end{bmatrix}^{\mathrm{T}} \in \mathbb{R}^{m+n}, \end{cases} \tag{30}$$

where Q_{ij} denotes the ijth element of $Q(t)$, and z_i denotes the ith element of $\mathbf{z}(t)$. To make the experiment work effectively, matrix $Q(t)$ is described as follows:

$$\begin{cases} Q_{ij}(t) = i + \sin(t), i = j, \\ Q_{ij}(t) = \frac{\sin(t)}{i-j}, i > j, \\ Q_{ij}(t) = \frac{\cos(t)}{i-j}, i < j. \end{cases}$$

Then, the vector $\mathbf{z}(t)$ is described as

$$\begin{cases} \mathbf{z}(t) = \sin(t), \text{ when } i \text{ is even} \\ \mathbf{z}(t) = \cos(t), \text{ when } i \text{ is odd.} \end{cases}$$

Besides, let both m and n be 10. For comparison, Newton-Raphson iterative (NRI) algorithm [30] and Z-type model [31] are introduced below.

- NRI algorithm:

$$\mathbf{x}_{k+1} = \mathbf{x}_k - Q_k^{-1}(Q_k\mathbf{x}_k - \mathbf{z}_k). \tag{31}$$

- Z-type model:

$$\mathbf{x}_{k+1} = 1.5\mathbf{x}_k - \mathbf{x}_{k-1} + 0.5\mathbf{x}_{k-2} + Q_k^{-1}\Big(\iota\dot{\mathbf{z}}_k - \iota\dot{Q}_k\mathbf{x}_k - \mu(Q_k\mathbf{x}_k - \mathbf{z}_k)\Big), \tag{32}$$

where μ denotes the step size. With the steady-state error $\|\mathbf{e}_k\|_2$ being the measure for the convergence performance of these algorithms, comparative results are shown in Figs. 1 through 3, and Table 1.

A. NOISE-FREE CONDITION

The accuracy of the model is an important indicator for evaluating the performance of a solving algorithm. Figure 1 evaluates the steady-state error of three models with different sampling periods under the noise-free condition. The results show that all three models converge. However, the proposed DTNSND model (11) possesses the smallest steady-state error, which is much smaller than those of the other two comparative models. Moreover, as shown in Table 1, when the sampling period ι decreases from 0.1 s to 0.01 s and then to 0.001 s, the maximal steady-state residual errors (MSSREs) generated by DTNSND model (11) exhibit a variation proportional to $O(\iota^2)$, decreasing from 8.988422×10^{-3} to 8.756398×10^{-6} and then to 8.762132×10^{-9}, which are smaller than those of comparative models, validating the correctness of Theorem 2. It is worth noting that truncation and rounding errors can introduce calculation noise even in the absence of external disturbances. In this regard, the proposed DTNSND model (11) demonstrates the superiority due to its noise suppression characteristics, and thus it outperforms the comparative models.

B. RANDOM NOISE CONDITION

In practical applications, random noise is typically caused by quantization error, measurement error, transmission error, and other factors. Although these errors can be minimized in the design and implementation of algorithms, they can still affect the performance of algorithms to some extent. In this subsection, a random noise $\zeta(t) = 5 \times [-1, 1]$ is introduced for the comparison between three different algorithms. Compared with the other two models, as shown in Fig. 2 and Table 1, DTNSND model (11) still exhibits excellent performance in accuracy. In contrast, both Z-type model (32) and NRI algorithm (31) display large steady-state errors at the order of 10^3, and thus they are less favorable than DTNSND model (11).

C. CONSTANT NOISE CONDITION

As illustrated in Fig. 3 and Table 1, even under the constant noise condition, the proposed DTNSND model (11) still exhibits with small steady-state error, almost the same as that under the noise-free condition. Besides, DTNSND model (11) has the MSSREs at the orders of 10^{-3}, 10^{-6}, and 10^{-9} for sampling periods of $\iota = 0.1$ s, $\iota = 0.01$ s, and $\iota = 0.001$ s, respectively. This finding is consistent with the analytical results of Theorem 3. By contrast, the comparative models have significant steady-state errors due to the effect of constant noise, which means that both models have low accuracy and poor robustness under the constant noise condition. Overall, the proposed DTNSND model (11) outperforms the other two models in terms of solution accuracy as well as robustness under the constant noise condition.

VII. EXTRACTION EXPERIMENTS

To further verify the noise suppression of DTNSND model (11), we acquire a remote sensing image of the Arctic sea ice

TABLE 1. MSSRE generated by Z-type model (32), NRI algorithm (31), and DTNSND Model (11) for solving Eq. (30) with different sampling periods under noise conditions.

ι (s)	Algorithm	MSSRE under different noise conditions		
		Noise-free $\zeta(t) = 0$	Random noise $\zeta(t) \in 5 \times [-1, 1]$	Constant noise $\zeta(t) = 100$
0.1	Z-type (32)	4.313642×10^{-1}	6.325087×10^{3}	8.240402×10^{2}
	NRI (31)	2.654581×10^{-1}	3.281694×10^{3}	3.279462×10^{2}
	DTNSND (11)	$\mathbf{8.988422 \times 10^{-3}}$	$\mathbf{8.240402 \times 10^{-1}}$	$\mathbf{8.988422 \times 10^{-3}}$
0.01	Z-type (32)	4.426232×10^{-2}	6.324835×10^{3}	6.324997×10^{2}
	NRI (31)	2.630418×10^{-2}	3.174315×10^{3}	3.173803×10^{2}
	DTNSND (11)	$\mathbf{8.756398 \times 10^{-6}}$	$\mathbf{9.074429 \times 10^{-1}}$	$\mathbf{8.756398 \times 10^{-6}}$
0.001	Z-type (32)	4.427403×10^{-3}	6.324310×10^{3}	6.324599×10^{2}
	NRI (31)	2.627958×10^{-3}	3.163786×10^{3}	3.163428×10^{2}
	DTNSND (11)	$\mathbf{8.762132 \times 10^{-9}}$	$\mathbf{9.666709 \times 10^{-1}}$	$\mathbf{8.762145 \times 10^{-9}}$

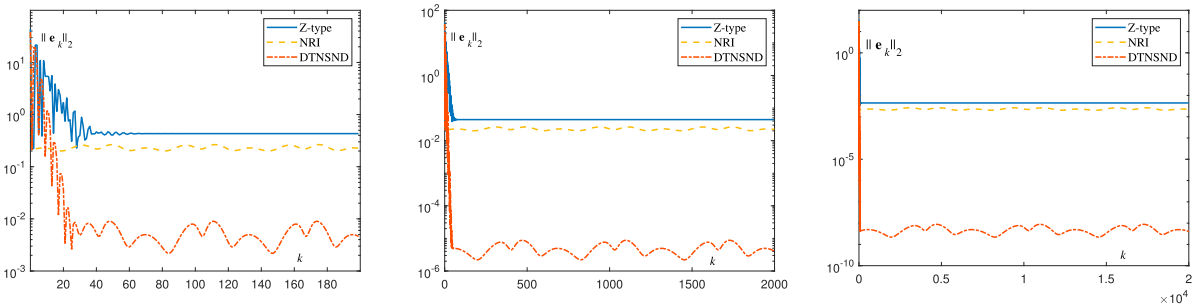

FIGURE 1. Steady-state error $\|e_k\|_2$ of Z-type model (32), NRI algorithm (31), and DTNSND model (11) under the noise-free $\zeta(t) = 0$ condition. (a) $\iota = 0.1$ s. (b) $\iota = 0.01s$ s. (c) $\iota = 0.001$ s.

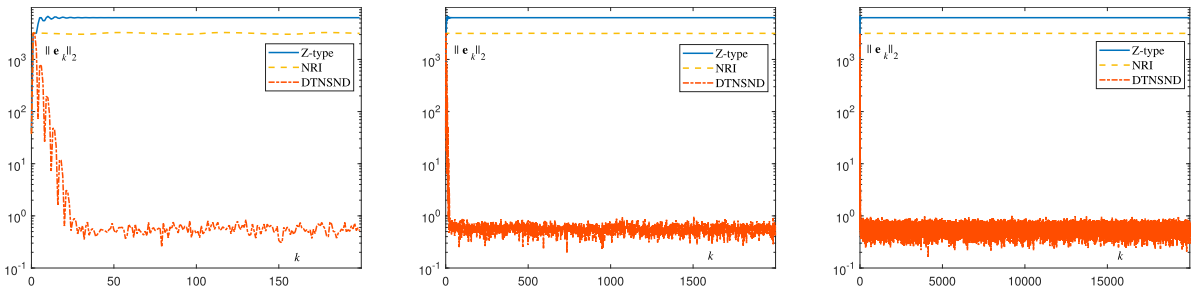

FIGURE 2. Steady-state error $\|e_k\|_2$ of Z-type model (32), NRI algorithm (31), and DTNSND model (11) under the random noise $\zeta(t) \in 5 \times [-1, 1]$ condition. (a) $\iota = 0.1$ s. (b) $\iota = 0.01$ s. (c) $\iota = 0.001$ s.

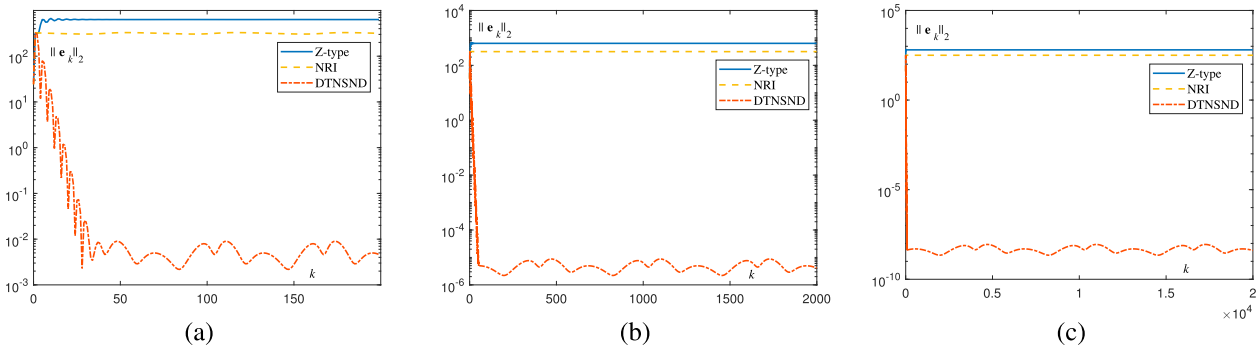

FIGURE 3. Steady-state error $\|e_k\|_2$ of Z-type model (32), NRI algorithm (31), and DTNSND model (11) under the constant noise $\zeta(t) = 100$ condition. (a) $\iota = 0.1$ s. (b) $\iota = 0.01$ s. (c) $\iota = 0.001$ s.

for the following extraction experiments under noise-free and random noise $\zeta(t) \in 5 \times [-1, 1]$ conditions. The remote sensing image is from HY-1C satellite, which is equipped with the Chinese ocean colour and temperature scanner. Extraction results are shown in Fig. 4 and Table 2.

A. DATASET AND EXPERIMENTAL PARAMETERS

Applying a preconditioned original remote sensing image of the Arctic sea ice as an experimental material, experiments are performed using MATLAB 2018b on a computer with Windows 11, AMD Ryzen 5 4600G, Radeon Graphics 3.70 GHz, and 16 GB RAM. In addition, to illustrate the excellent performance of DTNSND model (11) in detail, some of the indicators are discussed such as overall classification accuracy (OA), average classification accuracy (AA), product precision (PP), MSSRE, and Kappa coefficient. Then, their calculation formulas are listed below.

$$\begin{cases} \text{OA} = \frac{\text{TP+TN}}{\text{TP+FP+TN+FN}}, \\ \text{AA} = \frac{1}{2}(\frac{\text{TP}}{\text{TP+FN}} + \frac{\text{TN}}{\text{TN+FP}}), \\ \text{PP} = \frac{\text{TP}}{\text{TP+FP}}, \\ \text{Kappa} = \frac{p_0 - p_e}{1 - p_e}, \\ p_0 = \frac{\text{TP+TN}}{\text{TP+TN+FP+FN}}, \\ p_e = \frac{(\text{TP+FN})(\text{TP+FP}) + (\text{FP+TN})(\text{FN+TN})}{(\text{TP+TN+FP+FN})^2}. \end{cases}$$

According to the definition of the confusion matrix, TP, FP, TN, and FN mean true positive, false positive, true negative, and false negative, respectively.

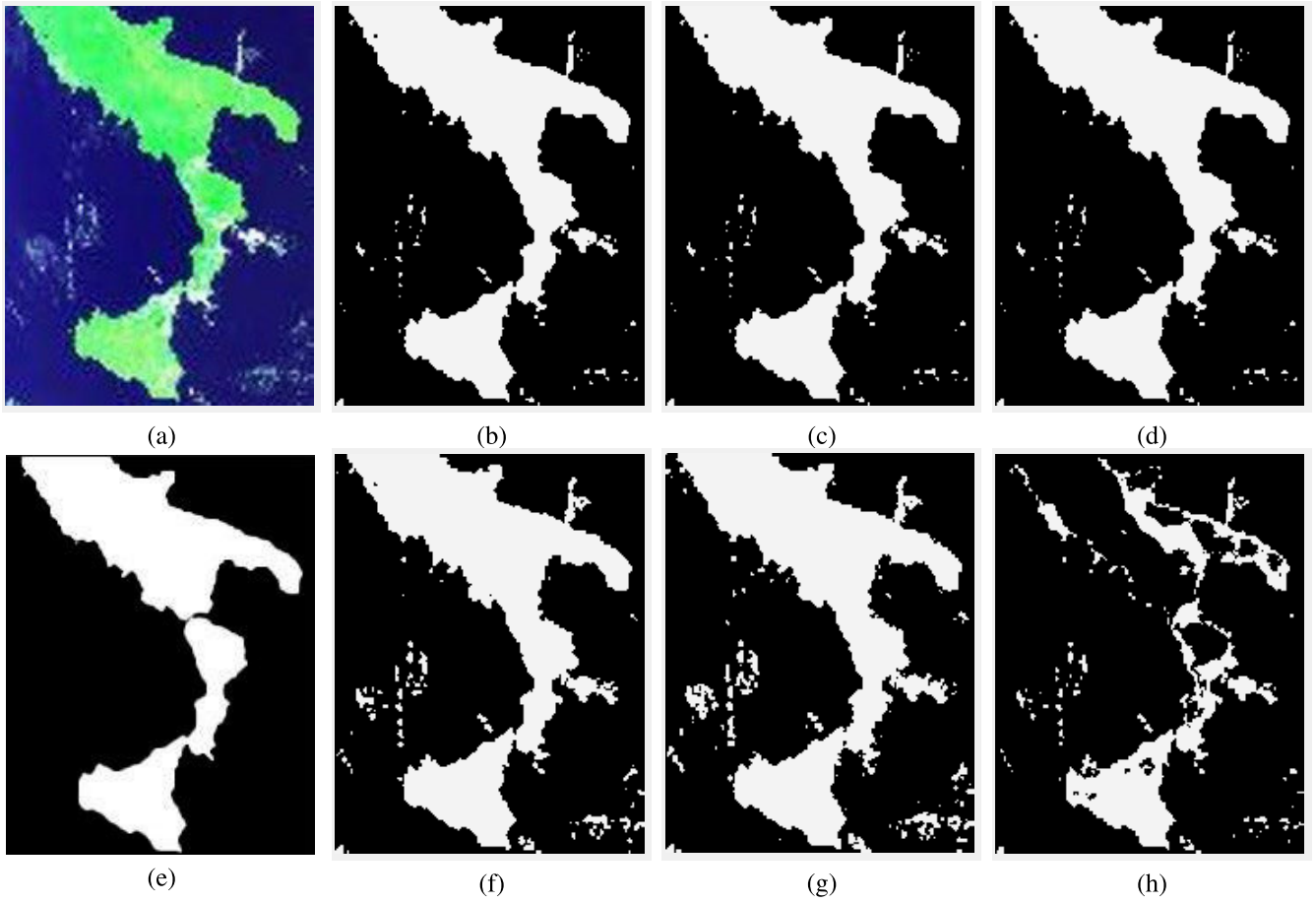

FIGURE 4. Results of CEM scheme (1) for the arctic sea ice extraction with three algorithms. (a) Original image. (b)-(d) Extraction results with DNSND model (11), NRI algorithm (31), and Z-type model (32) under the noise-free $\zeta(t) = 0$ condition. (e) Ground-truth image. (f)-(h) Extraction results with DNSND model (11), NRI algorithm (31), and Z-type model (32) under the random noise $\zeta(t) \in 5 \times [-1, 1]$ condition.

TABLE 2. Classification accuracy indicators and results of three algorithm-assisted CEM scheme (1) for the arctic sea ice: MSSRE, OA, AA, PP, and Kappa.

Accuracy Indicator	Noise-free $\zeta(t) = 0$			Random noise $\zeta(t) \in 5 \times [-1, 1]$		
	DNSND (11)	NRI (31)	Z-type (32)	DNSND (11)	NRI (31)	Z-type (32)
MSSRE	8.788956×10^{-14}	2.929643×10^{-14}	1.551863×10^{-13}	6.899219×10^{0}	9.058097×10^{0}	9.529840×10^{0}
OA	**0.970293**	**0.970293**	**0.970293**	**0.948761**	0.927637	0.844112
AA	**0.980305**	**0.980305**	**0.980305**	**0.965994**	0.952025	0.718403
PP	**0.892185**	**0.892185**	**0.892185**	**0.827571**	0.772578	0.817379
Kappa	**0.923019**	**0.923019**	**0.923019**	**0.870873**	0.822455	0.509556

B. COMPARISON OF EXTRACTION RESULTS

Figure 4(a) shows the original remote sensing image of the Arctic sea ice with a size of 174 × 255 pixels and a resolution of 50 m × 50 m. To visually compare the extraction results of three algorithms, Fig. 4(a) is first processed into a ground-truth image shown in Fig. 4(e). It can be observed from Fig. 4(b)-(d) that three algorithms to aid CEM scheme (1) show good performance in extraction experiments under the noise-free condition, and the Arctic sea ice can be accurately identified. Moreover, from Table 2, classification accuracy indicators for three algorithms are OA=0.970293, AA=0.980305, PP=0.892185, and Kappa=0.923019, identically. Besides, the MSSREs are of order 10^{-14}, 10^{-14}, and 10^{-13}, which shows that three algorithms have a high and similar convergence accuracy. In contrast, Fig. 4(f)-(h) illustrate the effects of three algorithms to extract the Arctic sea ice under the random noise $\zeta(t) \in 5 \times [-1, 1]$ condition. Distinctly, DTNSND model (11) still extracts the Arctic sea ice with essentially the same quality as the one under the noise-free condition, and the metrics in Table 2 can further support this result. On the contrary, there exist misidentifications on the left side in Fig. 4(g), while Fig. 4(h) has a large missing area. It means that NRI algorithm (31) and Z-type model (32) can not successfully overcome the perturbation of the noise in the solving process.

VIII. CONCLUSION

In this paper, we have constructed a DTNSND model for solving the QP problem converted from the CEM scheme, so as to extract the target from the optical remote sensing image. The proposed DTNSND model with an integration term suppresses the noise and finds optimal filter coefficients for the target extraction efficiently and stably. After conducting theoretical analysis and a series of numerical simulations, the noise suppression capabilities of the constructed model is confirmed, as well as its exceptional computational performance. Additionally, an experimental comparison of optical remote sensing image target extraction under different noise conditions was performed using an optical remote sensing image of the Arctic sea ice. The results demonstrated the high accuracy and strong stability of the DTNSND model.

ACKNOWLEDGMENT

The authors would like to thank NSOAS for providing the data free of charge. HY-1C data were obtained from https://osdds.nsoas.org.cn.

REFERENCES

[1] S. Sun, P. Zhong, H. Xiao, and R. Wang, "Active learning with Gaussian process classifier for hyperspectral image classification," *IEEE Trans. Geosci. Remote Sens.*, vol. 53, no. 4, pp. 1746–1760, Apr. 2015.

[2] J. Qi, Z. Gong, W. Xue, X. Liu, A. Yao, and P. Zhong, "An unmixing-based network for underwater target detection from hyperspectral imagery," *IEEE J. Sel. Topics Appl. Earth Observ. Remote Sens.*, vol. 14, pp. 5470–5487, 2021.

[3] J. Liu, Z. Wu, L. Xiao, J. Sun, and H. Yan, "A truncated matrix decomposition for hyperspectral image super-resolution," *IEEE Trans. Image Process.*, vol. 29, pp. 8028–8042, 2020.

[4] H. Fırat, M. E. Asker, M. İ. Bayındır, and D. Hanbay, "Hybrid 3D/2D complete inception module and convolutional neural network for hyperspectral remote sensing image classification," *Neural Process. Lett.*, pp. 1–44, 2022.

[5] J. C. Harsanyi and C.-I. Chang, "Hyperspectral image classification and dimensionality reduction: An orthogonal subspace projection approach," *IEEE Trans. Geosci. Remote Sens.*, vol. 32, no. 4, pp. 779–785, Jul. 1994.

[6] H. Ren and C.-I. Chang, "A target-constrained interference-minimized filter for subpixel target detection in hyperspectral imagery," in *Proc. IEEE Int. Geosci. Remote Sens. Symp. (IGARSS)*, Jul. 2000, pp. 1545–1547.

[7] D. E. Bar, K. Wolowelsky, Y. Swirski, Z. Figov, A. Michaeli, Y. Vaynzof, Y. Abramovitz, A. Ben-Dov, O. Yaron, L. Weizman, and R. Adar, "Target detection and verification via airborne hyperspectral and high-resolution imagery processing and fusion," *IEEE Sensors J.*, vol. 10, no. 3, pp. 707–711, Mar. 2010.

[8] E. Trentin, "Multivariate density estimation with deep neural mixture models," *Neural Process. Lett.*, pp. 1–16, Feb. 2023.

[9] W. Jiang, L. Ling, D. Zhang, R. Lin, and L. Zeng, "A time series forecasting model selection framework using CNN and data augmentation for small sample data," *Neural Process. Lett.*, pp. 1–28, Feb. 2023.

[10] L. Zong-ling, W. Lu-yuan, Y. Ji-yang, C. Bo-wen, H. Liang, J. Shuai, L. Zhen, and Y. Jian-feng, "Remote sensing ship target detection and recognition system based on machine learning," in *Proc. IEEE Int. Geosci. Remote Sens. Symp. (IGARSS)*, Jul. 2019, pp. 1272–1275.

[11] D. Zhang, J. Zhan, L. Tan, Y. Gao, and R. Župan, "Comparison of two deep learning methods for ship target recognition with optical remotely sensed data," *Neural Comput. Appl.*, vol. 33, no. 10, pp. 4639–4649, May 2021.

[12] W. Teng, N. Wang, H. Shi, Y. Liu, and J. Wang, "Classifier-constrained deep adversarial domain adaptation for cross-domain semisupervised classification in remote sensing images," *IEEE Geosci. Remote Sens. Lett.*, vol. 17, no. 5, pp. 789–793, May 2020.

[13] T. Zhang, Z. Wang, P. Cheng, G. Xu, and X. Sun, "DCNNet: A distributed convolutional neural network for remote sensing image classification," *IEEE Trans. Geosci. Remote Sens.*, vol. 61, 2023, Art. no. 5603618.

[14] J. Kang, R. Fernandez-Beltran, D. Hong, J. Chanussot, and A. Plaza, "Graph relation network: Modeling relations between scenes for multilabel remote-sensing image classification and retrieval," *IEEE Trans. Geosci. Remote Sens.*, vol. 59, no. 5, pp. 4355–4369, May 2021.

[15] X. Li, B. Liu, G. Zheng, Y. Ren, S. Zhang, Y. Liu, L. Gao, Y. Liu, B. Zhang, and F. Wang, "Deep-learning-based information mining from ocean remote-sensing imagery," *Nat. Sci. Rev.*, vol. 7, no. 10, pp. 1584–1605, Oct. 2020.

[16] W. Wu, S. Chen, and L. Bao, "A transfer learning algorithm based on support vector machine," *Neural Process. Lett.*, pp. 1–24, Dec. 2022.

[17] S. J. Pan and Q. Yang, "A survey on transfer learning," *IEEE Trans. Knowl. Data Eng.*, vol. 22, no. 10, pp. 1345–1359, Oct. 2010.

[18] J. C. Harsanyi, "Detection classification subpixel spectral signatures hyperspectral image sequences," Dept. Elect. Eng., Univ. Maryland, Baltimore, MD, USA, Tech. Rep., 1993.

[19] S. Chowdhury, D. K. Chao, T. C. Shipman, and M. A. Wulder, "Utilization of Landsat data to quantify land-use and land-cover changes related to oil and gas activities in west-central Alberta from 2005 to 2013," *GISci. Remote Sens.*, vol. 54, no. 5, pp. 700–720, Apr. 2017.

[20] X. Zhu, S. Li, X. Zhang, H. Li, and A. C. Kot, "Detection of spoofing medium contours for face anti-spoofing," *IEEE Trans. Circuits Syst. Video Technol.*, vol. 31, no. 5, pp. 2039–2045, May 2021.

[21] Z. Zhang, S. Chen, and S. Li, "Compatible convex–nonconvex constrained QP-based dual neural networks for motion planning of redundant robot manipulators," *IEEE Trans. Control Syst. Technol.*, vol. 27, no. 3, pp. 1250–1258, May 2019.

[22] Z. Marvi and B. Kiumarsi, "Barrier-certified learning-enabled safe control design for systems operating in uncertain environments," *IEEE/CAA J. Autom. Sinica*, vol. 9, no. 3, pp. 437–449, Mar. 2022.

[23] L. Jin, X. Zheng, and X. Luo, "Neural dynamics for distributed collaborative control of manipulators with time delays," *IEEE/CAA J. Autom. Sinica*, vol. 9, no. 5, pp. 854–863, May 2022.

[24] C. Hu, Y. Zhang, and X. Kang, "General and improved five-step discrete-time zeroing neural dynamics solving linear time-varying matrix equation with unknown transpose," *Neural Process. Lett.*, vol. 51, no. 2, pp. 1715–1730, Apr. 2020.

[25] Z. Zhang, T. Chen, L. Zheng, and Y. Luo, "A quadratic programming based neural dynamic controller and its application to UAVs for time-varying tasks," *IEEE Trans. Veh. Technol.*, vol. 70, no. 7, pp. 6415–6426, Jul. 2021.

[26] D. Chen, X. Cao, and S. Li, "A multi-constrained zeroing neural network for time-dependent nonlinear optimization with application to mobile robot tracking control," *Neurocomputing*, vol. 460, pp. 331–344, Oct. 2021.

[27] X. Xiao, D. Fu, G. Wang, S. Liao, Y. Qi, H. Huang, and L. Jin, "Two neural dynamics approaches for computing system of time-varying nonlinear equations," *Neurocomputing*, vol. 394, pp. 84–94, Jun. 2020.

[28] Y. Kong, Y. Jiang, R. Han, and H. Wu, "A generalized varying-parameter recurrent neural network for super solution of quadratic programming problem," *Neurocomputing*, vol. 437, pp. 238–248, May 2021.

[29] Y. Liufu, L. Jin, J. Xu, X. Xiao, and D. Fu, "Reformative noise-immune neural network for equality-constrained optimization applied to image target detection," *IEEE Trans. Emerg. Topics Comput.*, vol. 10, no. 2, pp. 973–984, Apr. 2022.

[30] W. Li and J. Swetits, "A Newton method for convex regression, data smoothing, and quadratic programming with bounded constraints," *SIAM J. Optim.*, vol. 3, no. 3, pp. 466–488, Aug. 1993.

[31] L. Jin, Y. Zhang, and B. Qiu, "Neural network-based discrete-time Z-type model of high accuracy in noisy environments for solving dynamic system of linear equations," *Neural Comput. Appl.*, vol. 29, no. 11, pp. 1217–1232, Jun. 2018.